

Flow measurements above a DBD plasma actuator array by means of defocusing PTV

Saskia Pasch*, Heinrich L. Lange, Robin Leister, Jochen Kriegseis

Institute of Fluids Mechanics, Karlsruhe Institute of Technology, Germany

*Corresponding author: saskia.pasch@kit.edu

Keywords: defocusing PTV, in-situ calibration, active flow control, DBD plasma actuator, 3D3C flow measurements, Lagrangian tracking.

ABSTRACT

Lagrangian defocusing particle tracking velocimetry (DPTV) measurements are conducted in a thin, wall-parallel volume above a plasma actuator array that is applied to mimic the effect of wall oscillations by inducing alternating, wall-parallel forcing in opposite directions into the air above the actuator surface. The aim of the experiments is to capture the plasma-induced flow structures in otherwise quiescent air in order to increase the understanding of different actuation parameters. For this purpose, high-speed particle image velocimetry equipment with one camera is used in a DPTV setup, where the out-of-plane particle coordinate is obtained through the diameter of a defocused particle image. On this basis, an approach for continuous particle tracking in several consecutive frames is presented, allowing to derive three component, three dimensional velocity and acceleration data. Light reflections that occur on the adjacent actuator surface give raise to particular challenges concerning the measurement uncertainty estimation as well as the calibration procedure for the evaluation of the wall-normal coordinate of tracer particles. To overcome the latter, a calibration approach is presented for which solid particles are applied to the actuator surface and their particle image diameter is captured at different camera positions in a separate measurement. The estimation of in-plane and out-of-plane displacement measurement uncertainties is conducted following a newly-developed procedure where the deviation of particle displacements from a straight track is evaluated for measurements in quasi-quiescent air. The obtained results show the suitability of DPTV measurement technique for the practical application of the characterization of flow structures above a plasma actuator array. The measurement accuracy is found to be limited due to the available illumination, which depends on the used components. The measured flow fields together with optical and electrical measurement data allow for a further analysis of the present forcing strategy. Particularly, by recording phase-resolved, three-dimensional flow velocity and acceleration fields in the vicinity of the wall, the spatio-temporal occurrence and homogeneity of the near-wall forcing effects can be analyzed in future investigations.

1. Introduction

Flow control strategies for turbulent skin-friction drag reduction have gained considerable interest due to their power saving potentials. Correspondingly, spanwise oscillating walls have been



Figure 1. Multi-electrode PA array for beat-frequency operation (Hehner et al., 2020).

shown to reduce surface drag in turbulent flows (Quadrio & Ricco, 2004; Marusic et al., 2021). As a simpler means of implementation of such strategies, arrays of dielectric barrier discharge (DBD) plasma actuators (PA) have been introduced to mimic the physical wall movement without previously required moving parts (Wilkinson, 2003; Jukes et al., 2006; Benard et al., 2019; Hehner et al., 2019, 2020).

DBD plasma discharges can occur when an alternating voltage difference that causes a sufficiently strong electric field is applied to two electrodes that are insulated from each other by a dielectric (Kogelschatz, 2003). This is accompanied by a mainly horizontal momentum input into the air above the lower, encapsulated electrodes (Benard & Moreau, 2014). An example for a DBD PA configuration is shown in Figure 1, where four different electrode groups, respectively supplied with the same voltage signal during operation, appear color-coded. The so-called beat frequency operation concept Hehner et al. (2020) uses such an actuator and builds upon the beat of the individual sinusoidal voltage signals between two neighboring electrodes. The resulting electrical potential difference causes alternating phases of plasma discharges and breaks. The spatial arrangement of electrodes and the accordingly applied individual voltages result in a temporal oscillation of the plasma discharges along both directions. This is indicated by the grey arrows in Figure 1.

To gain a deeper insight into the plasma-induced flow structures, and as an extension to the efforts of Hehner et al. (2022) of single-plane velocity measurements, defocusing particle tracking velocimetry (DPTV) measurement technique is employed for high-speed 3D3C velocity measurements in a thin volume parallel to the wall above the actuator. Thus, the wall-normal direction is not represented in the field of view but in the light sheet thickness, enabling volumetric measurements with only one camera by relating the particle image size of intentionally defocused particles with their wall-normal position along the optical axis of the camera. For the present measurements, calibration and uncertainty estimation procedures are discussed and a Lagrangian tracking approach is introduced. As a result, the captured three-dimensional tracks allow to evaluate the velocity and acceleration field in an entire volume above the actuator array. Together with the fluid-mechanical characteristics, the electrical voltage and current signals are monitored allowing an insight into the underlying interplay of the plasma discharges and the resulting forcing for different oscillation cycle phases.

Previously, simultaneous measurements of electrical and optical discharge characteristics were conducted for the PA array in BF mode (Pasch et al., 2023). An intensified charge coupled device (ICCD) camera allowed the observation of the instantaneous and statistical spatio-temporal structure of the discharge light emissions at different phases of the plasma and oscillation cycle. A planned combined evaluation of these efforts and the here-presented DPTV measurements is ex-

pected provide a comprehensive insight into the relations between the electrical properties of the discharges indicated in the current signal, their optical appearance and the corresponding fluid-mechanical impact for the rather complex forcing strategy of the BF mode at different actuation parameters.

2. Measurement technique

State of research

DPTV is based on the work of Willert & Gharib (1992) and enables to measure three-dimensional particle positions and velocities by associating the radius of a defocused particle image with the particle position along the optical axis. Therefore, as pointed out above, simple planar particle imaging velocimetry equipment with a thin laser light volume instead of a planar light sheet is used, albeit there is no commercial processing software available. Fuchs et al. (2016) presented an in-situ calibrated DPTV approach for wall-bounded volumes of several millimeters thickness. This procedure was later successfully applied by Leister et al. (Leister et al., 2021; 2023) for measurements of the oil-flow structure in an open wet clutch gap of a few hundred micrometers height. Lately, the suitability of DPTV for measurements in a turbulent channel flow (Leister et al., 2023) and the determination of wall-near turbulent flow structures and wall-shear-stress in a boundary layer flow (Fuchs et al., 2023) was shown.

Measurement principle

The main principle of this approach is the extraction of the depth position via the size of the defocused particle image. Figure 2 shows this principle for two particles – both positioned at different distances from the focal plane. Both particles form an out-of-focus particle image on the sensor chip of the camera.

Furthermore, the diameter of these images contains the explicit distance information to the focal plane. Note, the intensity of the image might be several orders-of-magnitude lower, than compared to an in-focus image as the same amount of light is distributed across a larger area on the camera chip. Olsen & Adrian (2000) derived a mathematical equation of this defocusing behavior under absence of optical aberration effects, which quantifies the interrelation between the particle size imaged on the sensor d_i with the physical diameter size of the particle d_p and can be formulated as

$$d_i^2 = M^2 d_p^2 + 5.95(M + 1)^2 \lambda^2 f_{\#}^2 + \frac{M^2 z^* D_a^2}{(s_o + z^*)^2}. \quad (1)$$

The first term describes the geometric particle image with the parameter M as magnification. The second term depicts the diffraction of light on the aperture of the lens, with λ as wave length of the light and $f_{\#}$ as focal number of the lens. The third term describes the diameter change of d_i caused by the distance z^* of the particle to the focal plane, the opening diameter of the aperture D_a and the parameter s_o , which describes the distance between the principal plane of the lens and the focal plane. Figure 3a shows a graphical implementation of this equation for two different particle diameters d_p . As already visually recognizable in said figure, the most dominant term of this equation is the third term, when considering particles with a certain distance to the focal plane. This fraction is a hyperbolic function with respect to z^* , but can be furthermore simplified to gain a linear interrelation, which can be written as

$$d_i = m_d z^* + d_0, \quad (2)$$

where d_0 is the particle image diameter at a known position, in our case, the wall and m_d the slope of the defocusing function.

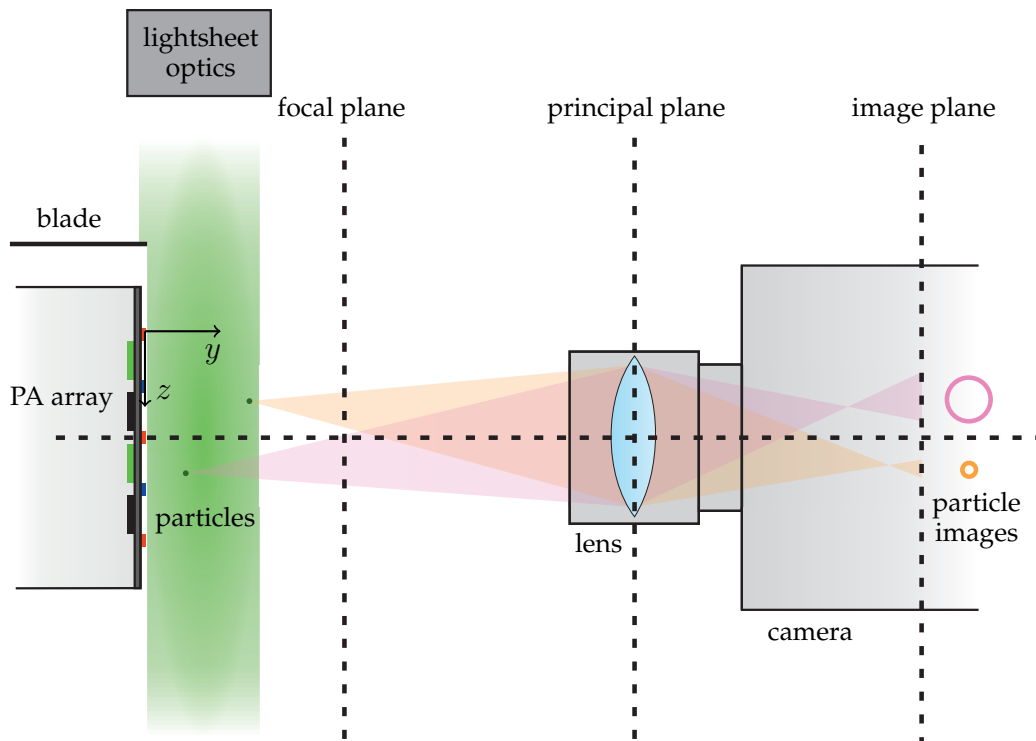


Figure 2. Detailed, not-to-scale sketch of measurement volume above PA and DPTV measurement principle.

Lagrangian DPTV

The used high-speed measurement equipment (see Section 3 for details) enables a continuous tracking of tracer particles using a constant Δt between two frames. Accordingly, the evaluation

algorithm based on the work of Leister et al. (2021) is adapted to find individual particle tracks in consecutive frames. As a consequence, Lagrangian particle tracks are detected and the fluid acceleration can be determined if two particle velocities or, respectively, three particle positions are evaluated.

Calibration Procedure

The application of DPTV above a PA array gives rise to specific challenges that require modification of the approaches presented previously (Fuchs et al., 2016, 2023, Leister et al., 2021; 2023). In particular, the measurement technique is sensitive to reflections of the laser light, which make it difficult to detect particles and gather velocity data especially in the vicinity of the wall. Furthermore, in a plasma-induced flow field, large velocity gradients occur in the near-wall region, raising particular interest in high resolution of the flow field in this region. The near-wall flow structures are also of key importance for possible future investigations of flow control mechanisms in turbulent flows. However, the actuator is mounted directly on the surface of the wall, so that transparent materials that might potentially avoid reflections such as glass must be excluded as a possible wall material. Although the application of several different surface coatings is tested, accessing the near-wall flow and observing no-slip particles remains challenging. The use of fluorescent particles, as to minimize the influence of wall reflections on the measurements, was not possible, especially with the equipment used because the light intensity would not have been sufficient. Consequently, the *in-situ* calibration procedure introduced by Fuchs et al. (2016) based on a linear fit of the velocity profile near the wall to identify the particle wall diameters with zero displacement can not be applied. Additionally, the here-regarded flow comprises only one wall, accordingly providing only one boundary condition for the determination the two calibration function constants. To overcome these restrictions, a calibration approach is developed based on the procedure presented by Fuchs et al. (2023).

The calibration was performed in a separate step using solid particles, which are applied to the PA array surface. For this purpose, *Lycopodiaceae* spores are used, which are advantageous due to their known, relatively constant size of around 30 μm (Giacosa et al., 2016). The transferability of the calibration with spores to the measurements with the Di-Ethyl-Hexyl Sebacat (DEHS) particles, which are one order of magnitude smaller, is feasible, as the influence of the particle diameter on the size of the particle image is negligible with sufficient defocusing. This effect is shown in Figure 3a, where the particle image diameter is plotted over the distance of the particle to the focus plane for particle diameters of 1 μm and 30 μm according to Equation 1. The distance range considered in the calibration and the measurement are marked in the plot in grey.

Instead of considering particle image diameters at different positions or wall-parallel planes within the measurement volume in the calibration, the camera is moved along the optical axis as per-

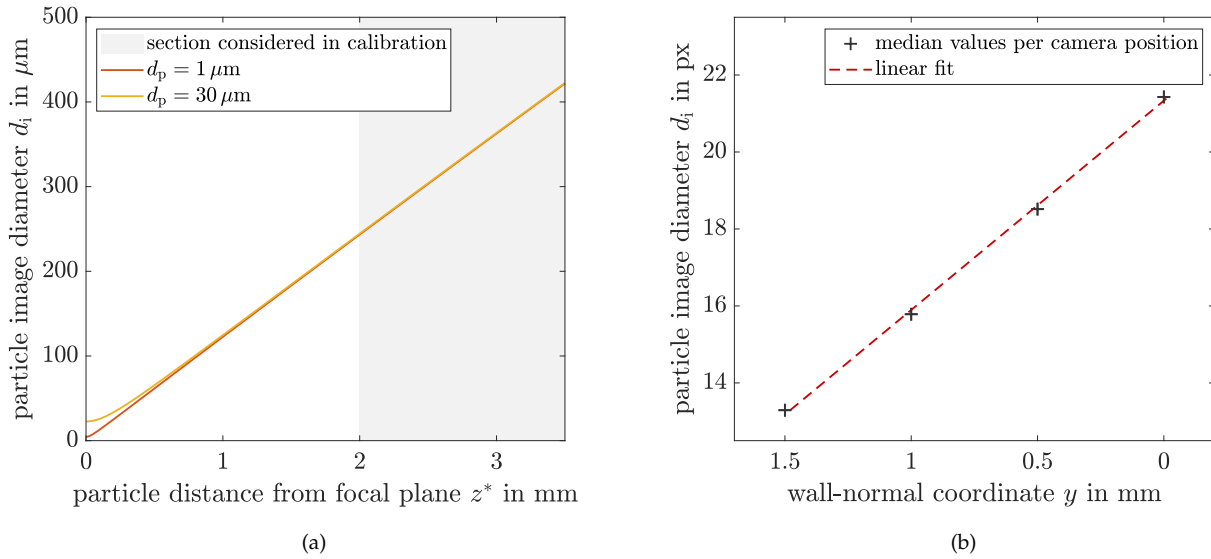


Figure 3. (a) Particle image diameter over distance of particle from focal plane according to equation introduced by Olsen & Adrian (2000) for particle diameters of DEHS ($1 \mu\text{m}$) and Lycopodiaceae ($30 \mu\text{m}$). (b) Calibration curve.

formed by Fuchs et al. (2023); Leister, Pasch, & Kriegseis (2023) on a fine-adjustment traverse and particle images are taken at different camera positions, i.e. distances of the particles to the focal plane, while the PA array and the laser light volume are kept stationary. A minimum of two camera positions and respective particle image diameters need to be considered to identify the two calibration parameters (cp. Equation 2). For the measurement shown here, particle images taken at four camera positions at 0.5 mm distance from each other are evaluated. The particle diameters are determined using an image processing procedure described in Section 4 and the median diameter value of all detected particles at one camera position was found. Figure 3b shows the obtained median particle image diameters for the assigned respective wall-normal distances from the focal plane in the measurement configuration. Subsequently, the calibration function indicated by the red dashed line is found by means of a linear fit of all four samples yielding a defocus sensitivity S^y of $184 \mu\text{m}/\text{px}$.

A calibration map assigning the wall position particle image diameter $d_0(x, y)$ to the x and y coordinate on the wall as introduced by Fuchs et al. (2016) can be created with the presented calibration approach, but was not considered for the present measurements, since it appeared as minor source of error. However, the particle image diameter was manually checked in different regions of the image using the camera software prior to the calibration measurements to avoid effects such as strong, systematic tilting of the camera relative to the PA.

Measurement uncertainty evaluation

The measurement accuracy depends on the uncertainty of the particle image diameter, in case of the out-of-plane coordinate along the optical axis, and position determination for the in-plane coordinates. These are influenced by the interplay of the chosen detection algorithm and image properties such as the signal-to-noise ratio (SNR) and the particle image size and resolution, which, in turn, depend on the used equipment and setup arrangement, the regularity of illumination and occurrence of reflections. Generally, a larger measurement uncertainty is observed for the out-of-plane velocity component in previous works (cp. e.g. Fuchs et al., 2016). In order to evaluate the measurement uncertainty quantitatively, Fuchs et al. (2016) were able to make the assumption of a planar flow with a known parabolic velocity profile function, which is not the case for the here-investigated flow. The presented approach allowed to evaluate the deviation of observed particle movement from the expected flow behaviour, which is then considered as measurement uncertainty. Due to the challenges described above for the here-presented measurements above the PA array in the immediate vicinity of the wall, already existing approaches could not be used and an alternative procedure need to be developed.

In a separate measurement, tracer particles are tracked in quasi-quiescent air at flow velocities close to 0 m/s in the configuration of the main measurements described later on in Section 3 above the actuator surface but without applying forcing. Over the duration of a short measurement, which was 2 s for the present experiment, a constant flow velocity is assumed and the observed deviations are consequently considered to occur mainly due to particle detection inaccuracies. Accordingly, the standard deviation of in-plane and out-of-plane particle displacement is determined as an estimation for the velocity measurement uncertainty. The observed tracks and practical details are given in Section 4.

3. Experimental setup and measurement procedure

Setup

The used PA array depicted in Figure 4b comprises five upper electrodes, each 1 mm wide, and four lower electrodes, each 3 mm wide, resulting in a total of eight discharge zones. Note, that the array is mounted with the x axis oriented horizontally and the z axis vertically, so that the coordinate system is rotated in following figures. To fabricate the upper electrodes, a conductive silver paint (sourced from *Holland Shielding Systems BV*) is applied to a polyethylene terephthalate (PET) foil, acting as a dielectric, using an airbrush pistol and a laser-cut adhesive stencil foil. Unlike for the shown actuator, the lower electrodes are made out of copper tape here instead of sprayed silver. In order to isolate the lower electrodes, a layer of polymer resin (specifically, *R&G 888658 HT2*) is encased within a 3D-printed frame, which is glued to the PET foil. Copper tape serves as

the electrical connections for the PA.

The experimental setup is mounted on an optical table to damp vibrations as shown in Figure 4a. The equipment for plasma generation and electrical measurements is assembled on the left side of the table and the measurement chamber with an extractor hood containing the components for the flow measurement covers the right table side. Plexiglas shields are installed on the aluminum frames of the extractor hood on all four sides to contain the seeding in the test rig area. An additional, smaller plexiglas box (not shown in the figure) with an opening on the side facing the camera is positioned around the PA to reduce the influence of external air flow in the room on the measurement results.

The upper HV electrode groups (shown in blue and red in Figure 1) are supplied by two Minipuls 1 HV transformers and the encapsulated electrodes (illustrated in green and black) are supplied by two Minipuls 2 HV transformers. The plasma frequencies applied to the upper electrode groups is $f_{ac,12} = 16$ kHz and to the lower encapsulated electrode groups $f_{ac,12} = 15.949$ kHz, yielding a beat and oscillation frequency of $f_{osc} = 51$ Hz. Voltage, current and trigger signals are captured simultaneously to the DPTV measurements, enabling the assignment of the exact phase within the plasma cycle of each measurement.

The PA array is attached to a vertical mounting platform with precision screws for fine adjustment of the pitch angle and horizontal position. As shown in Figure 2, the flat laser light volume is positioned parallel to the actuator, where the in-plane expansion in x and z direction of the actuator and the light volume is much greater than the horizontal light volume thickness in y direction. A horizontal blade is inserted above the PA mounting platform with precision screws for the y position in order to cut and align the laser volume with the actuator surface. The laser beam of a Nd:YLF high-speed laser (wavelength $\lambda = 527$ nm, pulse width < 210 ns) enters the measuring chamber from the top by means of a mirror arm and is fanned out using light sheet optics with an 8° cylindrical lens. The beam orientation can be aligned with the actuator by a slight rotation of the light sheet optics mount around the x axis. A camera (evaluated sensor section size of 512×512 pixel, 12 bit resolution) equipped with a $f = 50$ mm lens at $f_{\#} = 2$ aperture, and an additional distance ring of 12 mm captures DEHS particles ($1 \mu\text{m}$ diameter, Stokes number $Stk \approx 1, 5 \times 10^{-3}$) in the laser light volume. It is positioned opposite of the actuator using an electrical fine traverse for the horizontal direction (i.e. distance to the PA), a traverse for the vertical out-of-plane direction and an adjustment screw for the yaw orientation. The focal plane is positioned approximately 3.5 mm in front of the PA, in between the measurement volume and the camera. Accordingly, particles closer to the actuator are more defocused and appear larger in the image than particles at a greater distance from the actuator and closer to the focal plane. The measurements are taken at a magnification of 0.74, yielding a reproduction scale S^{xz} of $27 \mu\text{m}/\text{px}$. The exact model designation and manufacturer of all equipment components can be found in Table 1.

Measurement parameters and pre-experiment considerations

Prior to the experiments, a measurement parameter study is conducted to improve the acquisition of near-wall velocity information. In particular, the focus is to reduce reflections while still illuminating particles in the direct vicinity of the wall. Besides the fine adjustment of the components relative to each other, the PA array surface is coated with a thin layer of black color, which reduces reflections but possibly adds additional dielectric properties that might have a small influence on the plasma discharges. Additionally, the light sheet optics distance in negative z direction from the actuator (and thus the light volume width), the horizontal blade position and the horizontal PA position are varied systematically to optimize the measurements at a constant distance between camera and PA, i.e. defocusing level. The described efforts are directly linked to the achievable image illumination intensity of the used high-speed laser system, which is rather low in direct comparison to systems employed in the benchmark experiments (Fuchs et al., 2016; Leister et al., 2021) but, on the other hand, allows to track particles in multiple consecutive image frames. As described above, for DPTV the particle scattered light is distributed over a larger sensor area compared to acquisition of focused particles, which is accompanied by a lower SNR. Additionally, the pixel resolution of a particle image (which depends, among other things, on the camera used) and the available illumination limit the possible degree of defocusing, which directly influences the achievable measurement accuracy. To counteract the image illumination issue, the laser is employed in double pulse mode, i.e. the pulses of both cavities were operated simultaneously instead of alternatingly, to increase the light intensity at a constant pulse frequency of 1837 Hz (pulse distance of $\Delta t = 544.270 \mu\text{s}$), resolving the oscillation cycle in 36 phases.

4. Results and Discussion

Image processing and tracking algorithm

Before detecting and tracking the individual particle images, a pre-processing routine is applied in order to reduce artefacts of reflection, which mainly occur due to dust or the upper electrode borders, in the images and increase the SNR. In particular, the possible dynamic range of the sensor is only partially utilized for particle images. In a first step, background images are identified as moving median of 31 consecutive images symmetrically arranged around each individual image. The respectively identified background image is then weighted with the ratio of the average raw and background image intensity and subsequently subtracted from the raw image. Finally, the contrast is enhanced in the resulting images. An exemplary raw image and the image after performing the described pre-processing steps is given in Figures 5a and 5b. While the average image intensity of an exemplary raw image is 216, only 4 particle image pixel intensities exceed the value of 2000 and 1400 pixels assigned to reflections reach the saturation pixel intensity of 4096. After applying the

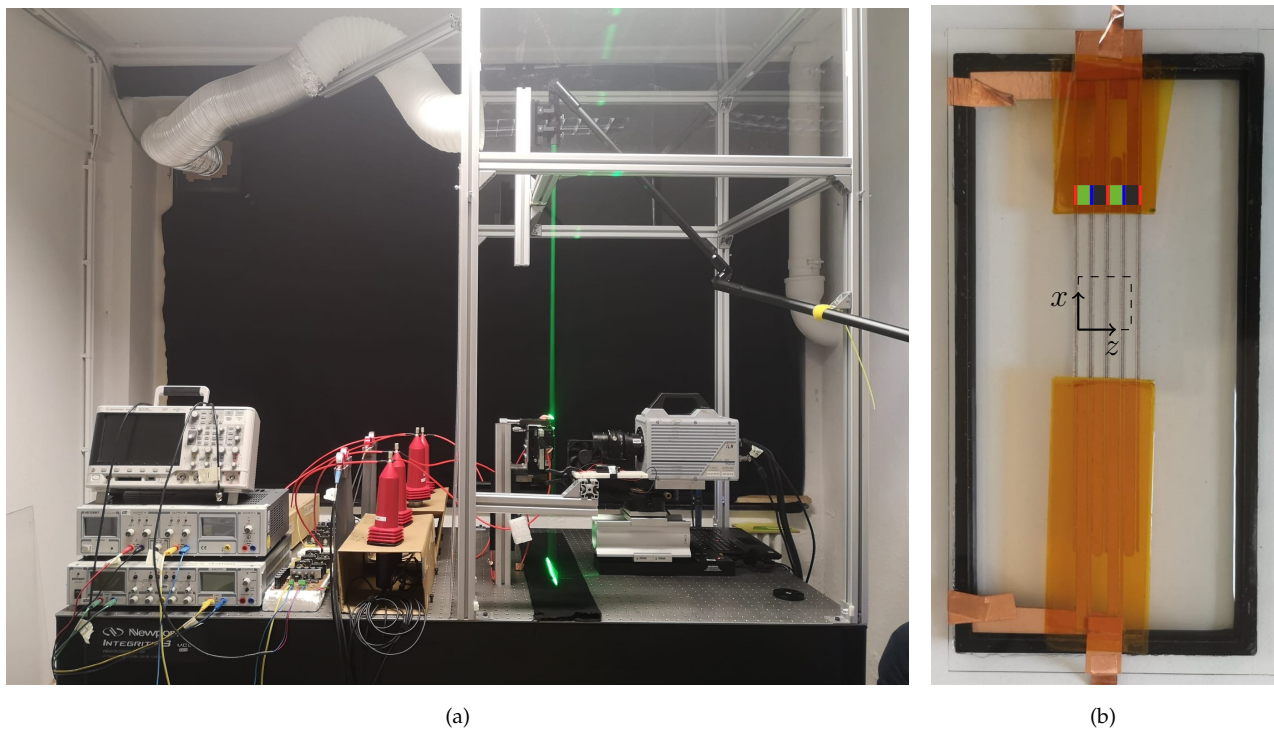


Figure 4. (a) Measurement setup comprising DC power supplies, HV transformers, coils for current measurements, HV probes for voltage measurement, laser light sheet optics, camera and PA array. (b) Detailed view of a similar PA array. The electrodes are shown by the color-coded blocks according to Fig. 1 and the camera field of view is marked by the dashed line.

pre-processing, the visibility of the particle images are clearly enhanced. Note that for the uncertainty estimation measurements in quasi-quiescent air a larger batch of 200 images is considered in the calculation of the moving-median-based background in order to distinguish between particle image and background intensity, because the particle movement is much slower. For the calibration the background images are taken in a separate measurement after the Lycopodium spores are removed.

As a next step, the particle images positions and diameters are identified for each individual image. The procedure and implementation for the particle image recognition are based on the Hough transformation Hough (1959) were largely adopted from Leister et al. (2021). An example for the detected circles for two particle images is shown in Figure 5c.

For the implementation of Lagrangian DPTV, the tracking algorithm used by Leister, Pasch, & Kriegseis (2023) suitable for tracking particle displacements of an image pair is expanded to enable the reconstruction of particle motion across multiple frames. For each particle image that is detected in one frame, a search is conducted in the subsequent frame within a defined maximum displacement range, similar to the nearest-neighbor approach. The expected displacement range is adjusted iteratively to the given flow and therefore chosen smaller for the quiescent air measurements than for the main experiments. If a match is found, the 3D particle position is added to the

Table 1. Components used in the experimental setup sorted by subsystems.

Setup component	Device and manufacturer
Plasma generation	
Function generator	Synchronizer control unit <i>ILA 5150 GmbH</i>
Power Supply	VLP-2403 Pro, VSP-2410, <i>VOLTCRAFT</i>
HV transformer	Minipuls 1, Minipuls 2, <i>GBS Elektronik GmbH</i>
Electrical measurements	
Oscilloscope	Picoscope 4424, <i>Pico Technology Ltd.</i>
HV probes	Pintek HVP-39pro, <i>Pintek Electronics Co., Ltd.</i>
Current transformer	Magnelab CT-C1.0 Rogowski coil, <i>Magnelab Inc.</i>
Optical measurements	
Laser	Darwin-Duo 527-100-M <i>Quantronix Corp.</i>
Laser beam propagation	Articulated Mirror Arm <i>ILA 5150 GmbH</i>
Light sheet optics	Standard Light Sheet Optics with cylindrical lens with effective focal length of 125 mm <i>ILA 5150 GmbH</i>
Lens	<i>Zeiss</i> $f = 50$ mm, $f^\# = 2$ and 12 mm distance ring
Camera	FASTCAM SA4, <i>Photron Deutschland GmbH</i>
Seeding generator	<i>PIVTEC GmbH</i>
Mechanical equipment	
Traverse System	Linear Translation Stage w. Integrated Controller, Stepper Motor <i>Thorlabs, Inc.</i>
Vibration damping	Optical table M-INT3 series <i>Newport Corporation</i>

track. The process is then repeated for the next frame. The track terminates if no suitable particle image is found or if multiple potential matches are detected. The outcome of this approach is the generation of trajectories of varying lengths. The procedure is performed for all particle images in all frames, that are not assigned to a track starting in previous frames.

Uncertainty estimation

As described in Section 2, a new approach is developed in order to evaluate the measurement uncertainty. Therefore, 3600 images taken in a separate measurement with setup, exposure time and laser frequency of the main experiments in quasi-quiescent air. Before performing these uncertainty evaluation measurements, the test-rig housing is closed and the setup left to rest for several minutes. The image pre-processing and tracking evaluation is conducted with the adjustments compared to the main measurements described above. From all identified tracks, 70 tracks for which particles were detected in 50 to 100 consecutively taken images are evaluated. As shown in

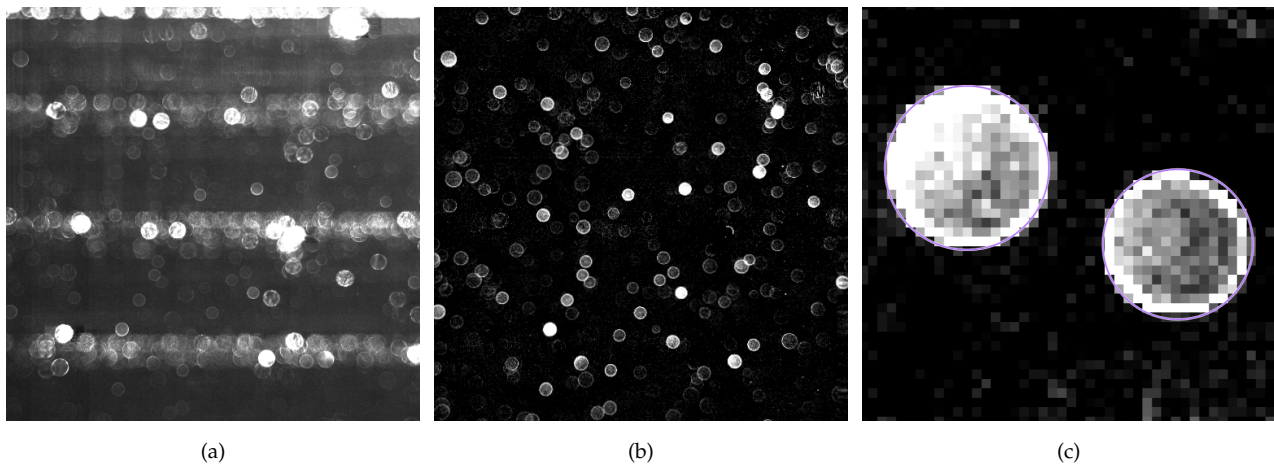


Figure 5. Illustration of image pre-processing and processing routine: (a) raw image, (b) image after background subtraction and contrast enhancement, (c) zoomed-in view of image section with two particle images with purple visualizes of the result of the particle image recognition using the Hough transform.

Figure 6, the particles are observed to move slowly along seemingly straight tracks. A closer look (cp. detail view of exemplary track in a volume of size $0.19 \text{ mm} \times 0.35 \text{ mm} \times 0.53 \text{ mm}$ in x , y and z direction), however, reveals that the detected particle positions fluctuate along these paths with the image acquisition frequency. The position of the electrodes is shown in the figure on the left, color-coding the different electrode groups as introduced in Section 1. The mean displacements in-between two frames were found to be 0.05 px in negative x direction, 0.12 px in negative z direction and 0.00008 px in diameter change, yielding an approximate absolute flow velocity of 6.4 mm/s . The displacement standard deviation, which is used as a measure for the displacement detection uncertainty, is found to be 0.33 px for in-plane particle displacements and 0.46 px for out-of-plane displacements in diameter change.

Measured flow Structures

190 000 particle tracks with minimum length of 3 frames are obtained from evaluating approximately 43 000 images which are taken in approximately 11.8 s representing 1200 oscillation cycles applying the routine described above. On average, 35 particles are detected in each image. The mean track length, i.e. the number of frames in which a particle is tracked, was 6 and the maximum track length 73.

Figures 7a and 7b shows 1500 and 5000 exemplary tracks color-coded according to their local z velocity in the y - z plane and x - z plane. The electrodes run at constant z values and the plasma forcing is expected to act mainly wall-parallel and perpendicular to the electrodes. In accordance with this, particle movement can be observed to occur mainly in z direction. It is furthermore clearly visible, that particles at high velocity gather close to the wall above the lower electrodes, i.e.

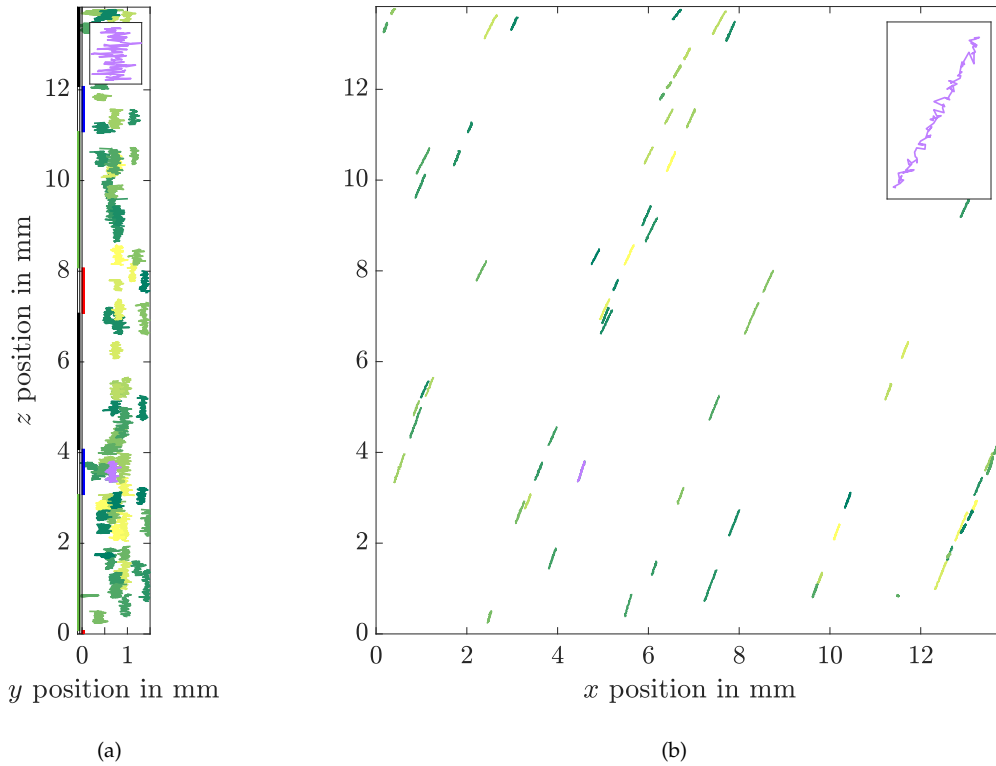


Figure 6. Particle tracks in almost quiescent air, (a) in y - z plane, (b) in y - z plane and zoomed-in view of particle track in highlighted in purple. Colors are chosen randomly to distinguish different tracks and do not indicate any information.

around $z \approx 2, 6$ and 10 mm, where the strongest forcing effect of the PA is expected. Additionally, the Figure visualizes where particles are detected more and less often. The occurrence of tracks fades uniformly from $y \approx 1$ mm with increasing wall distance, where the light volume and, thus, region of possible particle detection, ends. Less particles are also detected close to the wall and especially above the upper electrodes. This is to be expected due to the increasing size of particle images at larger distances from the focal plane and the occurrence of reflections especially above the upper silver electrodes, which exceed the dielectric surface.

In a next step, the collected flow data is projected on a grid, yielding phase-resolved velocity and acceleration fields. Velocity values are based on the particle displacement between two consecutive frames. Two successive particle displacements, or correspondingly three particle positions, result in one acceleration value. The velocity and acceleration data is assigned to the middle position and phase of the considered particles. Accordingly, the phase positions assigned to velocity and acceleration data are shifted by half a frame distance. In order to evaluate the velocity and acceleration fields assigned to one phase, 5 symmetric particle positions, i.e. 4 velocity and 3 acceleration values are considered. All values assigned to a the same grid cell and phase are averaged. The choice of parameters for the spatial grid and phase resolution allow to display the measurement

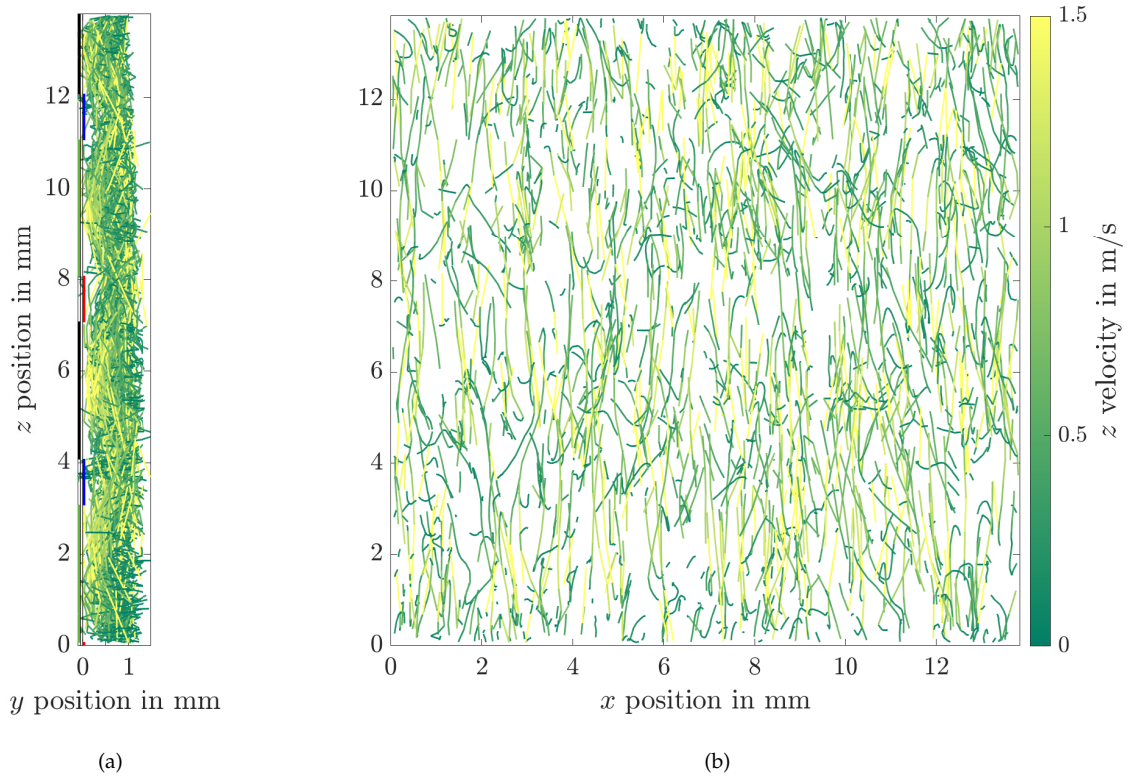


Figure 7. Particle tracks above operated PA array, (a) in y - z plane, (b) in x - z plane. Brighter colors indicate higher z velocity.

results from different perspectives. Figure 8 shows the z -component acceleration distribution as contour plot and the in-plane components velocity distribution as vector arrows for six out of 36 phases within the oscillation cycle. All detected tracks are considered in the evaluation and the measurement volume is divided into 15 bins in y and 40 bins in z direction, yielding respective spatial resolutions of 1 mm and 0.35 mm. No partition of the measurement volume in x direction (i.e. out-of-plane direction in the figure) is considered. A velocity or acceleration value is assigned to a grid cell when at least 40 data points were detected in the respective cell. As already indicated in Figure 7a, the density of detected particles decreases towards the wall due to a decreasing SNR at increasing level of defocusing further away from the focal plane as well as reflections that particularly occur above the elevated upper electrodes. However, especially in the region in the left of Figure 8 for z values between 9 mm and 13 mm in the given coordinate system, an almost continuous velocity and acceleration field is observed for the chosen grid where the values closest to the wall represent the flow at a wall distance of 50 μm .

For the flow fields shown in Figure 9, the same procedure is applied for a grid with 14 cells in x and z direction and an according spatial resolution of approximately 1 mm in both directions. Different from the procedure above, the shown flow field represents only the lower third of the

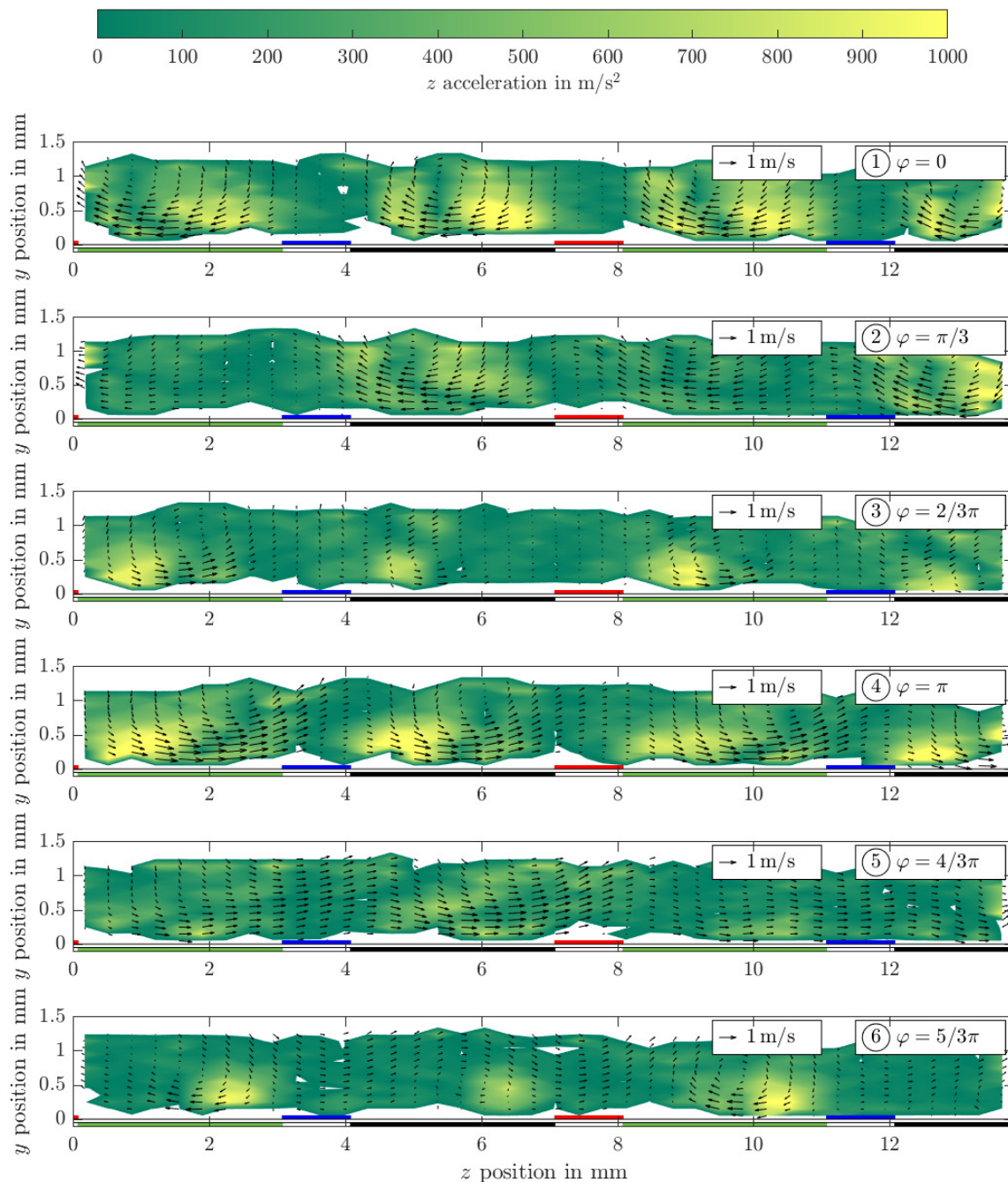


Figure 8. Phase-averaged y - and z -velocity and z -acceleration field indicated by vector arrows and color-coded contours in y - z plane for six exemplary oscillation phases. Brighter colors indicate higher z acceleration.

measurement volume from the PA array up to 500 μm above it, as the flow field is known to change strongly along the wall-normal direction (cp. Figure 8). Due to the increased total number of grid cells, the minimum number of values per grid cell is reduced to 25 in order to yield a mostly continuous flow field representing the near-wall layer.

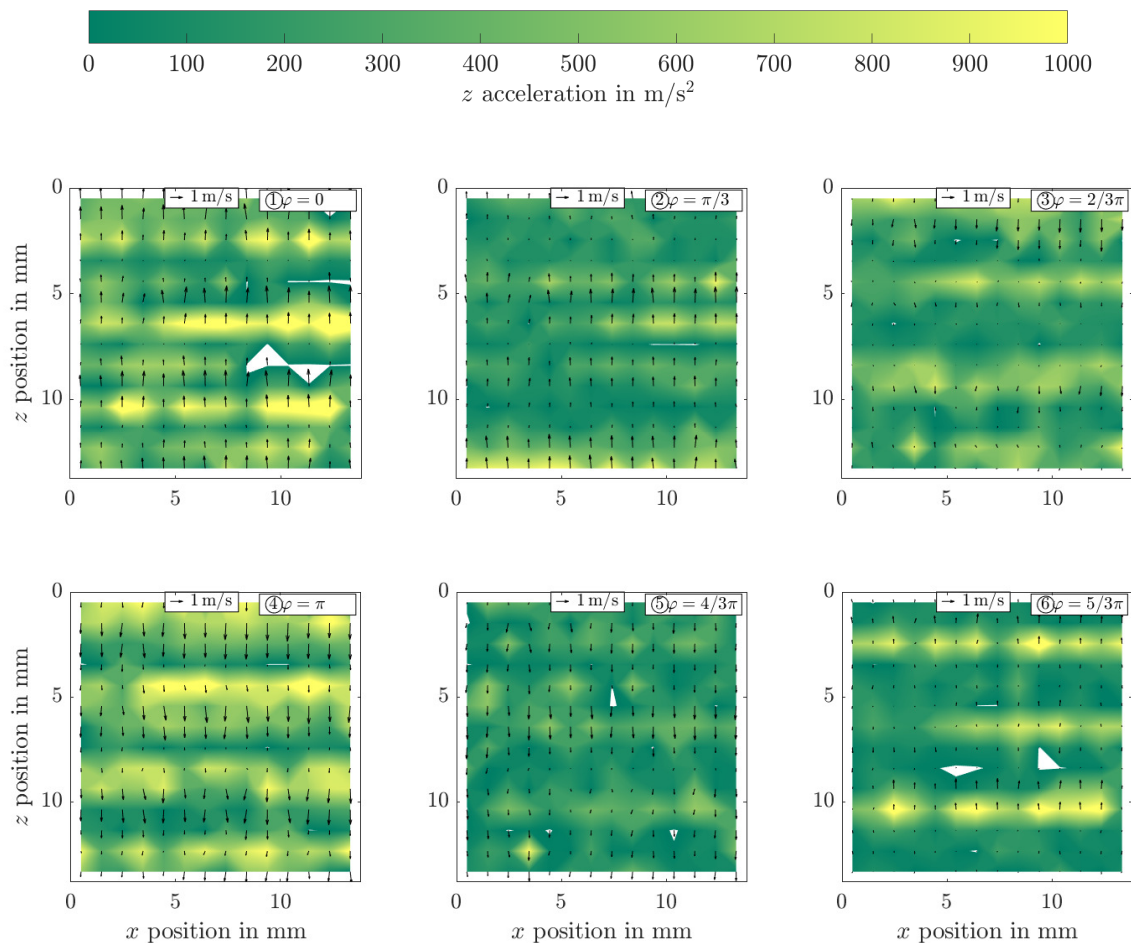


Figure 9. Phase-averaged x - and z -velocity and z -acceleration field indicated by vector arrows and color-coded contours in x - z plane representing the velocity data detected in a 500 μm thick volume above the PA array for six exemplary oscillation phases. Brighter colors indicate higher z acceleration.

The observed velocity and acceleration fields illustrate the region and direction of the plasma-based forcing starting at the edges of the upper electrodes in the region above the encapsulated electrodes in approximately wall-parallel (z) direction (cp. phases 1 and 3 in Figures 8 and 9, respectively). Over the course of one oscillation cycle, the forcing strength decreases and, eventually, the forcing direction reverses. Both perspectives on the plasma-induced flow fields emphasize the symmetric character of the oscillation cycle. In particular, phases 1 and 3, 2 and 4, as well as 3 and 6 show a similar but oppositely oriented behaviour respectively. This indicates that the applied voltages are balanced, which is an important requirement for the development of the plasma-based

implementation of the oscillating wall effects.

5. Conclusions and Outlook

DPTV measurement technique is applied to measure the flow in a wall-bounded region above a PA array. It is shown that 3D3C velocity and acceleration data can be determined by introducing a continuous tracking approach and an ex-situ calibration method, for which no prior knowledge or velocity data in the direct vicinity of the wall is required. For these conditions, a new procedure for the estimation of the measurement uncertainty is presented based on additional measurements in quasi-quiescent air. Since calibration and uncertainty estimation must be carried out in separate steps, the overall effort increases. However, the described adaptations allow the practical applicability of the measurement technique in an unknown flow situation.

The estimated measurement uncertainty, especially for the out-of-plane displacement which is reconstructed based on the change of the particle image diameter, of the applied setup is found to be comparably large. This observation can be associated with the used high-speed measurement components, which are required for the evaluation of continuous particle tracks and, correspondingly, acceleration values. In particular, for a limited illumination intensity of the laser, the defocus sensitivity is limited by the decreasing SNR that occurs for particle images at an increasing particle image diameter. On the other hand, the minimum possible particle image size is given by the applicability of the Hough transform in the image detection algorithm. The pixels of the used camera are comparably large, which is advantageous for the illumination level but, in turn, reduces the pixel resolution of the particle images and limits the applicability of existing image processing approaches for DPTV.

The conducted volumetric measurements of all three velocity and acceleration components reveal the spatial distribution and temporal course of the developing flow structures, providing a valuable insight into the effects of (plasma-based) forcing strategies. In particular, the insight into the flow fields close to the wall can be of great benefit for the development of turbulent flow control strategies. Furthermore, the data allows for a combined analysis of the spatio-temporal relation between optical emissions of discharges and the observed footprint in the flow in ongoing investigations.

References

Benard, N., Bayoda, K. D., Bonnet, J. P., & Moreau, E. (2019). Non homogeneous streamwise wall forcing by surface plasma actuator. *European Drag Reduction and Flow Control Meeting*.

- Benard, N., & Moreau, E. (2014). Electrical and mechanical characteristics of surface AC dielectric barrier discharge plasma actuators applied to airflow control. *Exp. Fluids*, 55(11). doi: 10.1007/s00348-014-1846-x
- Fuchs, T., Bross, M., & Kähler, C. J. (2023). Wall-shear-stress measurements using volumetric μ PTV. *Experiments in Fluids*, 64(6), 115. doi: 10.1007/s00348-023-03656-1
- Fuchs, T., Hain, R., & Kähler, C. (2016). In situ calibrated defocusing PTV for wall-bounded measurement volumes. *Measurement Science and Technology*, 27(8), 084005. doi: 10.1088/0957-0233/27/8/084005
- Giacosa, J. R., Morbelli, M., Giudice, G., & Gorrer, D. (2016). Spore morphology and wall ultra-structure of Lycopodiaceae from northwest Argentina. *Review of palaeobotany and palynology*, 225, 84–94. doi: /10.1016/j.revpalbo.2015.11.009
- Hehner, M. T., Gatti, D., Kotsonis, M., & Kriegseis, J. (2022). Effects of actuation mode on plasma-induced spanwise flow oscillations. *Journal of Physics D: Applied Physics*, 55(20), 205203. doi: 10.1088/1361-6463/ac526b
- Hehner, M. T., Gatti, D., & Kriegseis, J. (2019). Stokes-layer formation under absence of moving parts—A novel oscillatory plasma actuator design for turbulent drag reduction. *Physics of Fluids*, 31(5). doi: 10.1063/1.5094388
- Hehner, M. T., Gatti, D., Mattern, P., Kotsonis, M., & Kriegseis, J. (2020). Virtual wall oscillations forced by a DBD plasma actuator operating under beat frequency - a concept for turbulent drag reduction. In *Aiaa aviation 2020 forum* (p. 2956). doi: 10.2514/6.2020-2956
- Hough, P. V. (1959). Machine analysis of bubble chamber pictures. In *International conference on high energy accelerators and instrumentation, cern, 1959* (pp. 554–556).
- Jukes, T., Choi, K.-S., Johnson, G., & Scott, S. (2006). Turbulent drag reduction by surface plasma through spanwise flow oscillation. In *3rd aiaa flow control conference* (p. 3693). doi: 10.2514/6.2006-3693
- Kogelschatz, U. (2003). Dielectric-Barrier Discharges: Their History, Discharge Physics, and Industrial Applications. *Plasma chemistry and plasma processing*, 23(1), 1–46. doi: 10.1023/A:1022470901385
- Leister, R., Fuchs, T., & Kriegseis, J. (2023). Defocusing PTV applied to an open wet clutch: from macro to micro. *Experiments in Fluids*, 64(5), 94. doi: 10.1007/s00348-023-03623-w

- Leister, R., Fuchs, T., Mattern, P., & Kriegseis, J. (2021). Flow-structure identification in a radially grooved open wet clutch by means of defocusing particle tracking velocimetry. *Experiments in fluids*, 62(2), 1–14. doi: 10.1007/s00348-020-03116-0
- Leister, R., Pasch, S., & Kriegseis, J. (2023). Defocusing PTV in a turbulent channel flow – near-wall characteristics. In *15th international symposium in particle image velocimetry*.
- Marusic, I., Chandran, D., Rouhi, A., Fu, M. K., Wine, D., Holloway, B., ... Smits, A. J. (2021). An energy-efficient pathway to turbulent drag reduction. *Nature Communications*, 12(1), 5805. doi: 10.1038/s41467-021-26128-8
- Olsen, M., & Adrian, R. (2000). Out-of-focus effects on particle image visibility and correlation in microscopic particle image velocimetry. *Experiments in fluids*, 29(Suppl 1), 166–174. doi: 10.1007/s003480070018
- Pasch, S., Fridlender, T., Hehner, M. T., Benard, N., & Kriegseis, J. (2023). Combined and simultaneous electro-optical diagnostics for oscillatory plasma discharges. In *Aiaa aviation 2023 forum* (p. 4027). doi: 10.2514/6.2023-4027
- Quadrio, M., & Ricco, P. (2004). Critical assessment of turbulent drag reduction through spanwise wall oscillations. *Journal of Fluid Mechanics*, 521, 251–271. doi: 10.1017/S0022112004001855
- Wilkinson, S. P. (2003). Investigation of an oscillating surface plasma for turbulent drag reduction. *41st Aerospace Sciences Meeting & Exhibit, 2003-1023*. doi: 10.2514/6.2003-1023
- Willert, C., & Gharib, M. (1992). Three-dimensional particle imaging with a single camera. *Experiments in Fluids*, 12(6), 353–358. doi: 10.1007/BF00193880